The Astronomical Journal, 163:295 (16pp), 2022 June https://doi.org/10.3847/1538-3881/ac6ac8

The μ Arae Planetary System: Radial Velocities and Astrometry

G. F. Benedict[1], B. E. McArthur[1], E. P. Nelan[2], R. Wittenmyer[3], R. Barnes[4], H. Smotherman[4], and J. Horner[3]
[1] McDonald Observatory, University of Texas, Austin, TX 78712, USA; fritz@astro.as.utexas.edu
[2] Space Telescope Science Institute, Baltimore, MD 21218, USA
[3] Centre for Astrophysics, University of Southern Queensland, Toowoomba Qld 4350, Australia
[4] University of Washington, Seattle, WA 98195, USA
Received 2021 August 4; revised 2022 April 22; accepted 2022 April 25; published 2022 May 27

Abstract

With Hubble Space Telescope Fine Guidance Sensor astrometry and published and previously unpublished radial velocity measures, we explore the exoplanetary system μ Arae. Our modeling of the radial velocities results in improved orbital elements for the four previously known components. Our astrometry contains no evidence for any known companion but provides upper limits for three companion masses. A final summary of all past Fine Guidance Sensor exoplanet astrometry results uncovers a bias toward small inclinations (more face-on than edge-on). This bias remains unexplained by small number statistics, modeling technique, Fine Guidance Sensor mechanical issues, or orbit modeling of noise-dominated data. A numerical analysis using our refined orbital elements suggests that planet d renders the μ Arae system dynamically unstable on a timescale of 10^5 yr, in broad agreement with previous work.

Unified Astronomy Thesaurus concepts: Exoplanets (498)

Supporting material: machine-readable tables

1. Introduction

Multiple-planet systems provide an opportunity to probe the dynamical origins of planets (e.g., Ford 2006). Every multiple-planet system has the potential to serve as a case study of planetary system evolution (Wright et al. 2009). They provide laboratories within which to tease out the essential processes and end states from the accidental. μ Arae is such a system.

The μ Arae system is one of the best known multiplanet systems, with components having received official IAU names in late 2015. Butler et al. (2001) announced the discovery of μ Arae b, which was initially thought to move on an eccentric orbit. Pepe et al. (2007) presented new observations of the μ Arae system, revealing the four components known today. Using Doppler spectroscopy, that team announced the discovery of component c and firmed up the period of component e. This multiplanet system has until now only minimum masses for the four components (with periods 9.6 days $< P <$ 3900 days; Pepe et al. 2007). With access to only radial velocity (RV) observations, the inferred masses depend on their orbital inclination angle, i, providing minimum mass values, $0.03 < \mathcal{M} \sin i < 1.8$ $\mathcal{M}_{\rm Jup}$, for the four companions found by RV. Hence, we included this system in a Hubble Space Telescope (HST) proposal (Benedict 2007) to carry out astrometry using the Fine Guidance Sensors (FGS). Those observations supported attempts to establish true component mass and the architectures of several promising candidate systems, all relatively nearby, and with companion $\mathcal{M} \sin i$ values and periods suggesting measurable astrometric amplitudes.

For μ Arae we follow analysis procedures previously employed for the exoplanetary systems υ And (McArthur et al. 2010), HD 136118 (Martioli et al. 2010), HD 38529 (Benedict et al. 2010), HD 128311 (McArthur et al. 2014), and HD 202206 (Benedict & Harrison 2017). μ Arae companion masses and the μ Arae system architecture were our ultimate goals. Unfortunately, our astrometric investigation of μ Arae yields only a parallax consistent with the Gaia EDR3 values. Based on the astrometric residual statistics, we estimate upper mass limits for components μ Arae b, d, and e. These limits are consistent with both the Gaia precision and the lack of acceleration obtained from a comparison of Hipparcos and Gaia EDR3 proper motions (Brandt 2021).

Section 2 identifies the sources of RV and our modeling results. Section 3 describes the astrometric data and modeling techniques used in this study. After determining parallax and proper motion, we subject the residuals to periodogram analysis and find no significant signals at any of the periods determined from the RV (Section 4). Our astrometric precision yields only upper limits on possible companion masses. We discuss these results in comparison to past FGS astrometric results (Section 5) and briefly revisit system stability in Section 6. Lastly, in Section 7 we summarize our findings.

Table 1 contains previously determined information and sources for the host star subject of this paper, μ Arae. We abbreviate millisecond of arc as mas throughout and state times as mJD = JD –2,400,000.

2. μ Arae Radial Velocities

Pepe et al. (2007) reported previous and new RVs, components of the stellar orbital motion around the barycenter of the system, with Doppler spectroscopy. We list all RV data with sources in Table 2. We take the CORALIE RVs from Pepe et al. (2007). To these we add new publicly available data from the HARPS spectrograph on the 3.6 m ESO telescope at La Silla (Trifonov et al. 2020). We also include 180 RV measurements from the UCLES spectrograph (Diego et al. 1990) on the 3.9 m Anglo-Australian Telescope, gathered as part of the 18 yr Anglo-Australian Planet Search program (e.g.,

Table 1
μ Arae Stellar Parameters

Parameter	Value	Source[a]
SpT	G3IV−V	1
$T_{\rm eff}$	5773 K	6
log g	4.2 ± 0.1	6
[Fe/H]	0.28 ± 0.03	6
Age	5.7 ± 0.6 Gyr	5
Mass	1.13 ± 0.02 $\mathcal{M}_\odot$	5
Distance	15.57 ± 0.02 pc	2
Radius	1.33 ± 0.02 $R_\odot$	5
$v \sin i$	3.1 ± 0.5 km s^{-1}	7
$m - M$	0.961 ± 0.005	2
V	5.15 ± 0.01	1
K	3.68 ± 0.25	3
$V - K$	1.47 ± 0.25	1, 3

Note.
[a] 1 = SIMBAD; 2 = this paper; 3 = 2MASS; 5 = Bonfanti et al. (2015); 6 = Soto & Jenkins (2018); 7 = Fischer & Valenti (2005).

Table 2
Radial Velocities[a]

mJD[b]	RV	RVerr	Residual	Source[c]
52,906.5194	−9.29090	0.00118	0.00516	11
53,160.7260	−9.33980	0.00070	0.00105	11
53,161.7278	−9.34280	0.00070	0.00017	11
53,162.7260	−9.34480	0.00070	0.00038	11
53,163.7259	−9.34770	0.00070	−0.00130	11
53,164.7258	−9.34820	0.00070	−0.00220	11
53,165.6828	−9.34550	0.00070	−0.00086	11
53,166.7820	−9.34270	0.00070	0.00036	11
53,167.7269	−9.34210	0.00070	0.00018	11
53,201.6199	−9.36110	0.00119	−0.00091	11
53,202.6414	−9.35980	0.00119	0.00114	11
53,203.6108	−9.36190	0.00119	−0.00175	11
…	…	…	…	…

Notes.
[a] All velocity units in km s^{-1}.
[b] mJD = JD −2,400,000.
[c] 11 = HARPS1 (Pepe et al. 2007); 12 = CORALIE (Pepe et al. 2007); 14 = AAT (Tinney et al. 2001; Wittenmyer et al. 2014, 2017) and this paper; 15 = HARPS2 (Lo Curto et al. 2015).

(This table is available in its entirety in machine-readable form.)

Tinney et al. 2001; Wittenmyer et al. 2014, 2017). For all data sets, where there were multiple observations in a single night, we binned them together using the weighted mean value of the velocities in each night. We adopted the quadrature sum of the rms about the mean and the mean internal uncertainty as the error bar of each binned point.

This changing velocity, v, is the projection of a Keplerian orbital velocity to the observer's line of sight plus a constant velocity, γ. K is the velocity semiamplitude in km s^{-1}. The total RV signal we model includes contributions from all components. Because our GaussFit modeling results critically depend on the input data errors, we first modeled the RV to assess the validity of the original input RV errors. Achieving a χ^2/dof of unity for our solution required increasing the original errors on the RVs by a factor of 1.4 for CORALIE and UCLES and by 2.0 for HARPS. This suggests either that the errors were underestimated or that that the fit is not as good as it could be (i.e., evidence that there may be more to learn about the system). Figure 1 presents RV plotted as a function of time and the final combined orbital solution. The rms residual is 3.8 m s^{-1}. Table 3 contains derived velocity offsets for each RV source. Table 4 contains orbital elements and 1σ errors for components b, c, d, and e based on these RVs.

μ Arae has always presented stability challenges (Pepe et al. 2007; Timpe et al. 2013; Laskar & Petit 2017; Agnew et al. 2018). Given the frequency with which intrinsic stellar activity has been found to mimic a Keplerian signal in RV data (e.g., Robertson et al. 2014, 2015; Rajpaul et al. 2016; Díaz et al. 2018), we examined the available activity indicators from the HARPS spectra for μ Arae to determine whether or not all RV signals are dynamical, not stellar activity.

We obtained the complete set of activity indicators from the recently released HARPS RVBANK (Trifonov et al. 2020), which has corrected for nightly zero-point offsets and other systematics. The available indicators are FWHM, bisector, Hα, and the two Na D lines. Using the online *Agatha* tool[5] (Feng et al. 2017), we computed four periodograms (Bayes factor, maximum likelihood, Bayesian generalized least squares, and generalized least squares) for each of these activity-indicator time series to search for activity-related signals. The only significant periodicities were those near 1 yr (357–368 days), with the bisectors alone showing a significant peak at 497 days. Thus, none of the RV signals attributed to μ Arae companions can be attributed to line profile distortion due to stellar activity.

3. μ Arae Astrometry

Unless otherwise noted, for μ Arae we carried out exactly the same analysis detailed in Benedict & Harrison (2017) for HD 202206.

3.1. Astrometric Data

For this study astrometric measurements came from Fine Guidance Sensor 1r (FGS 1r), an upgraded FGS installed in 1997 during the second HST servicing mission.

We utilized only the fringe tracking mode (POS mode; see Benedict et al. 2017 for a review of this technique) in this investigation. POS mode observations of a star have a typical duration of 60 s, during which over 2000 individual position measurements are collected. We estimate the astrometric centroid by choosing the median measure, after filtering large outliers (caused by cosmic-ray hits and particles trapped by Earth's magnetic field). The standard deviation of the measures provides a measurement error. We refer to the aggregate of astrometric centroids of each star secured during one visibility period as an "orbit." We identify the astrometric reference stars and science target in Figure 2. Figure 3 shows the final measured location pattern within FGS 1r.

We present a complete ensemble of time-tagged μ Arae and reference star astrometric measurements, OFAD[6] and intra-orbit drift-corrected, in Table 5, along with calculated parallax factors in R.A. and decl.. These data, collected from 2007 May to 2010 April, in addition to providing material for confirmation of our results, could ultimately be combined with Gaia measures to significantly extend the time baseline of the

[5] https://phillippro.shinyapps.io/Agatha
[6] The optical field angle distortion (OFAD) calibration (McArthur et al. 2006).

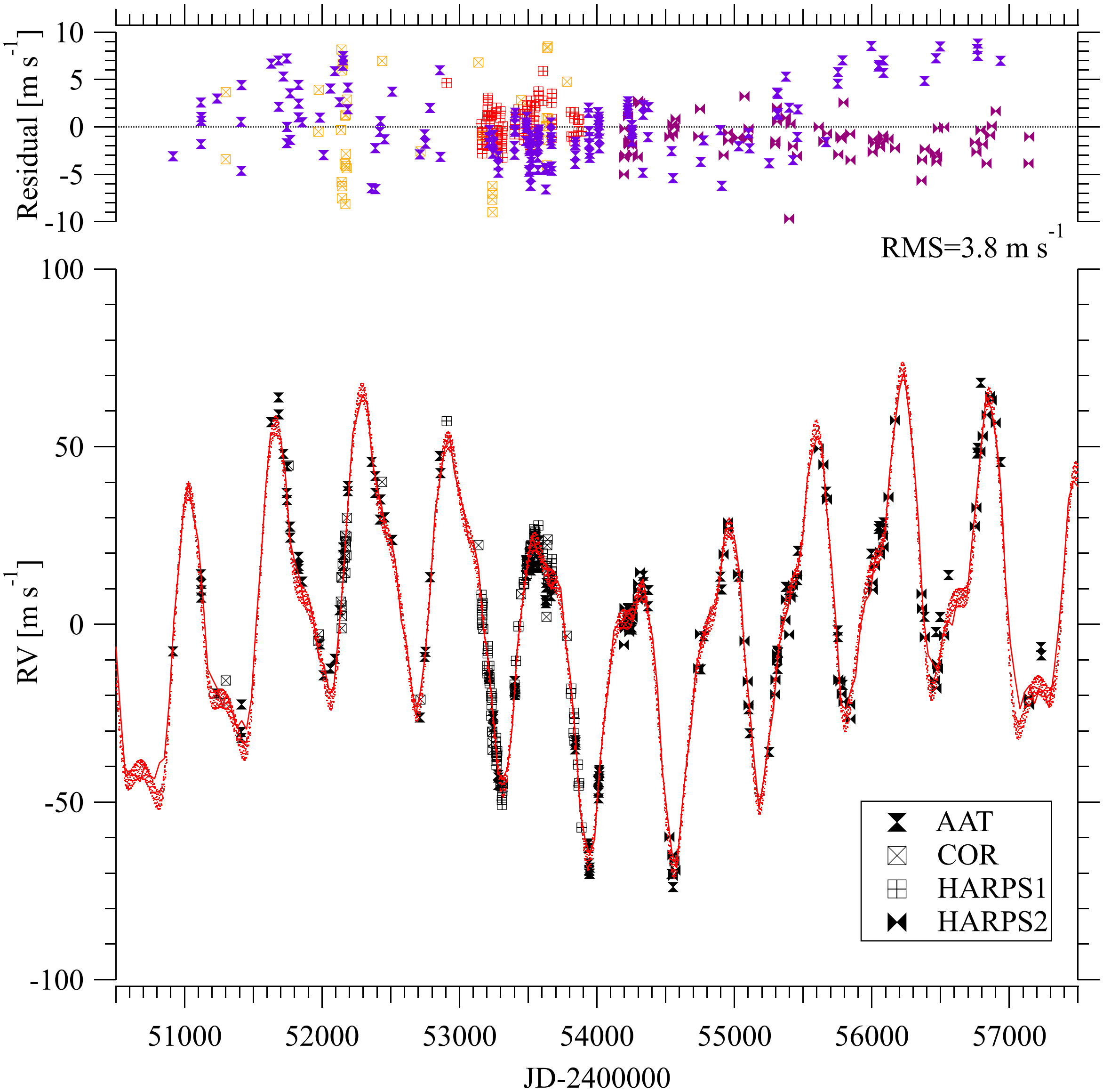

Figure 1. RV values from the sources listed in Table 2 plotted on the final RV four-component orbit (Table 4). All RV input errors have been increased by a factor of 1.4 to achieve a near-unity χ^2. Residuals are plotted in the top panel. We note the rms RV residual value in the plot.

Table 3
RV Offsets

RV Source	γ (m s^{-1})
CORALIE	−9379.1 ± 0.9
HARPS1	−9348.1 0.2
AAT	−7.6 0.3
HARPS2	1.7 0.2

astrometry, thereby improving proper-motion and perturbation characterization.

3.2. Astrometry Modeling Priors

As in all of our previous FGS astrometry projects (e.g., Benedict et al. 2001, 2007, 2011, 2016; Benedict & Harrison 2017; McArthur et al. 2010, 2011), we include as much prior information as possible in our modeling. We utilize parallax, proper-motion, cross-filter, and lateral color calibration priors in this analysis.

Past investigations (e.g., Harrison et al. 1999; Benedict et al. 2011) derived reference star parallaxes from a combination of photometry and spectroscopy. In support of this approach we obtained spectroscopy of the reference stars, long before the publication of Gaia EDR3. We used the RC Spectrograph on the CTIO Blanco 4 m. The Loral 3K CCD detector with KPGL1-1 grating delivered a dispersion of 1.0 Å pixel^{-1}, covering the wavelength range 3500 Å $< \lambda <$ 5830 Å. Classifications used a combination of template matching and line ratios. We estimate spectral types (included in Table 6 for completeness) with precision generally better than ±2 subclasses.

To check the luminosity classes obtained from classification spectra and the Gaia EDR3 parallaxes (Gaia Collaboration et al. 2021), we obtain proper motions from the EDR3 for a 1 deg^2 field centered on μ Arae and then produce a reduced proper-motion diagram (Stromberg 1939; Gould & Morgan 2003; Yong & Lambert 2003) as additional confirmation. Figure 4 contains the reduced proper-motion diagram for the

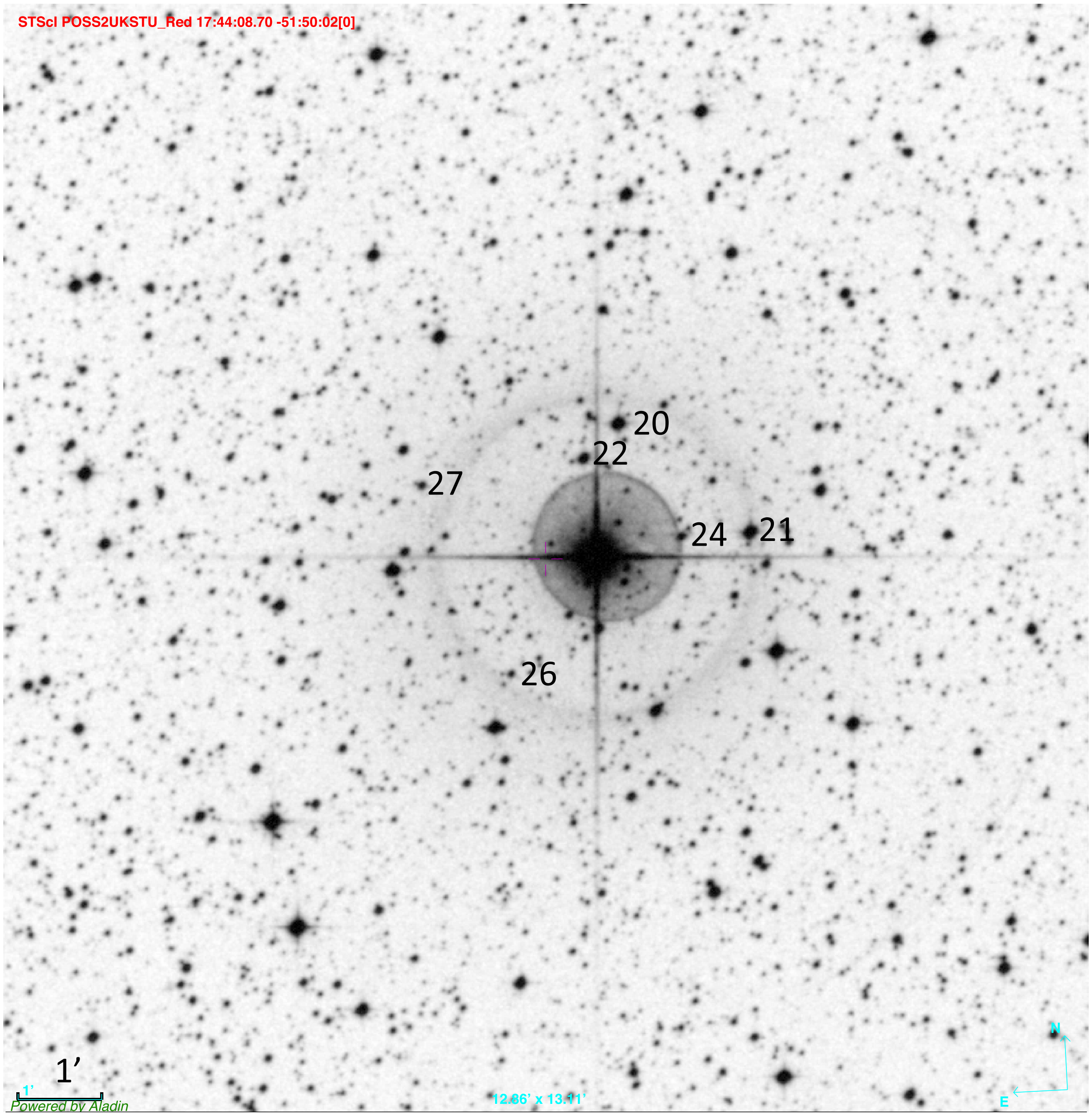

Figure 2. μ Arae and the astrometric reference stars (20–27) identified in Table 6.

Table 4
Orbital Elements for the μ Arae *b*, *c*, *d*, *e* Perturbations, Radial Velocity Only

Parameter	*b*	*c*	*d*	*e*
P (days)	645.0 ± 0.3	9.6392 ± 0.0006	307.9 ± 0.3	3947 ± 23
P (yr)	1.7664 0.0008	0.026391 0.000002	0.8429 0.0008	10.81 0.06
T (mJD)	52,396 28	52 4	52,720 9	53,264 388
ϵ	0.036 0.007	0.16 0.06	0.091 0.014	0.022 0.012
K (m s^{-1})	36.1 0.2	2.94 0.17	12.23 0.27	22.18 0.25
ω (deg)	39 16	197 20	193 10	84 36

μ Arae field, including μ Arae and our reference stars. We employ the following priors:

1. *Parallax:* Rather than rely on spectrophotometric reference star parallax estimates, this investigation simply adopts EDR3 values (Gaia Collaboration et al. 2021). It should be noted, however, that we do not treat those values as being hardwired or absolute. Instead, we consider them to be quantities (Table 6) introduced as observations with error. The average EDR3 parallax error is 0.02 mas. We also list the renormalized unit weight error (RUWE) for each reference star. Stassun & Torres (2021) find that the Gaia RUWE robustly predicts

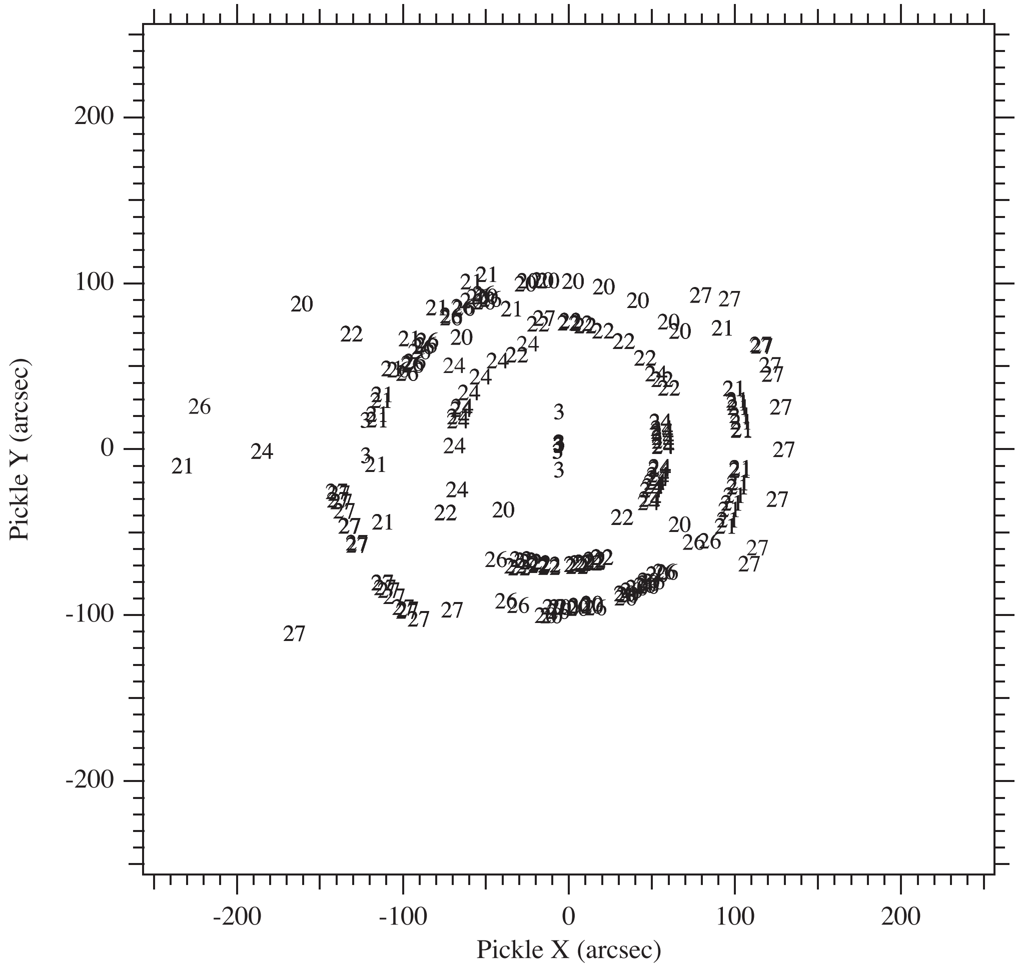

Figure 3. Positions of μ Arae (3) and astrometric reference stars (20–27) in FGS 1r FOV coordinates.

Table 5
μ Arae Field Astrometry[a]

Set	Star	HSTID	V3 Roll	X	Y	σ_X	σ_Y	$t_{\rm obs}$	P_α	P_δ
1	3	F9YM3703M	143.36	−6.35877	2.36891	0.00162	0.00179	54289.5332	−0.547823	−0.446584
1	3	F9YM370DM	143.36	−6.35864	2.36810	0.00164	0.00195	54289.5430	−0.548134	−0.446536
1	3	F9YM3709M	143.36	−6.35758	2.37029	0.00157	0.00182	54289.5390	−0.548009	−0.446558
1	3	F9YM370KM	143.36	−6.35756	2.36914	0.00154	0.00174	54289.5505	−0.548353	−0.446493
1	20	F9YM3707M	143.36	60.02043	75.67643	0.00203	0.00224	54289.5375	−0.547843	−0.446125
1	20	F9YM370CM	143.36	60.02464	75.67678	0.00210	0.00230	54289.5422	−0.547992	−0.446101
1	21	F9YM370FM	143.36	−58.68031	99.86974	0.00209	0.00172	54289.5446	−0.549343	−0.446231
1	21	F9YM3705M	143.36	−58.67832	99.87097	0.00197	0.00211	54289.5356	−0.549057	−0.446278
1	21	F9YM370AM	143.36	−58.67787	99.87108	0.00195	0.00202	54289.5399	−0.549194	−0.446257
1	22	F9YM3708M	43.36	56.18870	40.94541	0.00218	0.00198	54289.5383	−0.547666	−0.446275
1	22	F9YM3702M	143.36	56.18970	40.94592	0.00234	0.00209	54289.5324	−0.547478	−0.446300
1	22	F9YM370LM	43.36	56.18984	40.94558	0.00241	0.00238	54289.5513	−0.548056	−0.446201
1	22	F9YM370EM	143.36	56.19062	40.94591	0.00213	0.00205	54289.5437	−0.547839	−0.446245
1	26	F9YM370IM	143.36	−30.61732	−95.19696	0.00247	0.00302	54289.5482	−0.547849	−0.446956
1	26	F9YM3704M	143.36	−30.61421	−95.19866	0.00279	0.00284	54289.5344	−0.547419	−0.447030
1	27	F9YM370JM	143.36	113.50825	−60.51056	0.00223	0.00225	54289.5495	−0.546776	−0.446515
2	3	F9YM3809M	148.22	−5.44870	2.63273	0.00193	0.00191	54293.4618	−0.647938	−0.433618
2	3	F9YM380PM	148.22	−5.44869	2.63362	0.00184	0.00183	54293.4778	−0.648432	−0.433538
…	…	…	…	…	…	…	…	…	…	…

Note.
[a] Set (orbit) number, star number (#3 = μ Arae; reference star numbers same as Table 6), HST orbit and target identifier, spacecraft +V3 axis roll angle as defined in Chapter 2, FGS Instrument Handbook (Nelan 2015), OFAD-corrected X and Y positions in arcsec, position measurement errors in arcsec, time of observation = JD–2400000.5, R.A. and decl. parallax factors. We provide a complete table in the electronic version of this paper.

(This table is available in its entirety in machine-readable form.)

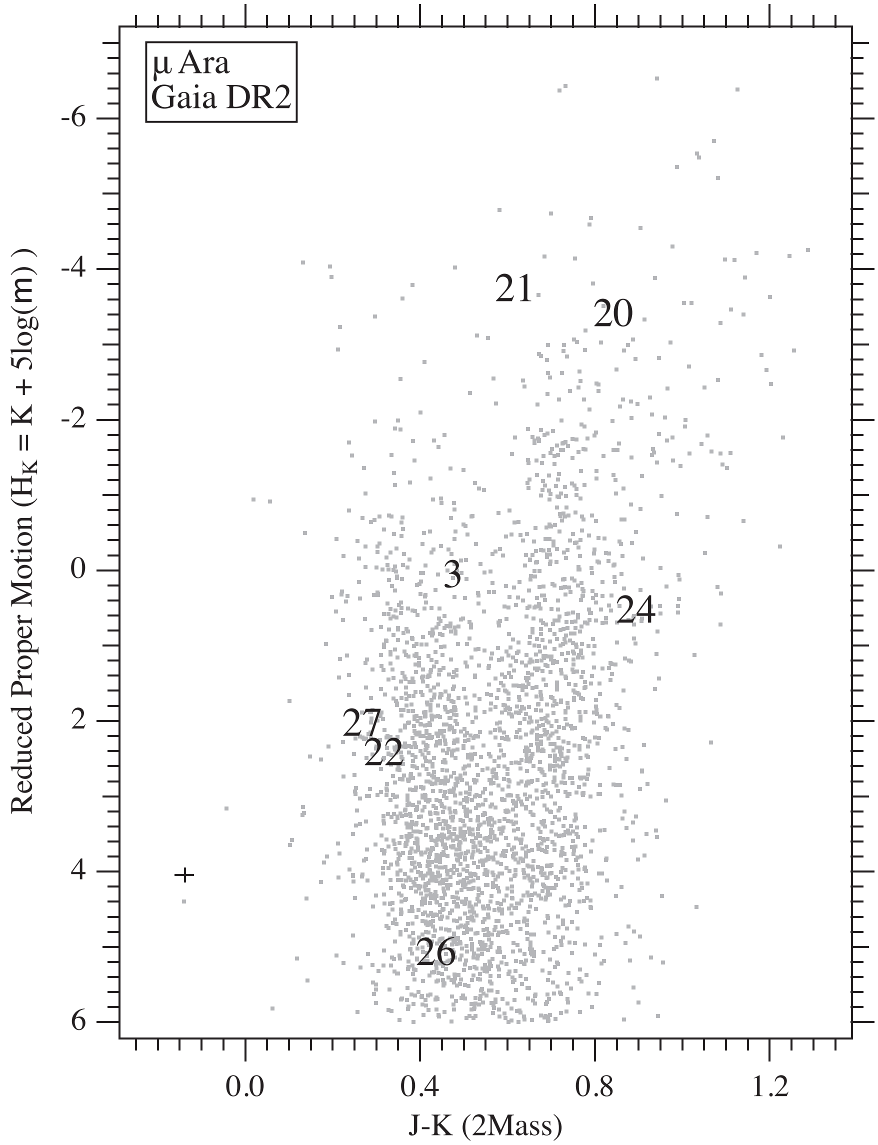

Figure 4. Reduced proper-motion diagram for 3200 stars in a 1° field centered on μ Arae, #3 on the plot. Star identifications are in Table 6, and proper motions are from Gaia DR2. For a given spectral type, giants and subgiants have more negative H_K values and are redder than dwarfs in $(J-K)$. The small plus sign at the lower left represents a typical $(J-K)$ error of 0.04 mag and H_K error of 0.17 mag.

Table 6
Parallax Priors for μ Arae Astrometric Reference Stars

Ref Star #	V[a]	$B-V$	SpT[b]	EDR3 Source	G	ϖ [c]	RUWE[d]
20	12.22	1.50 ± 0.03	K3III	5946035772071080000	11.6655	0.48 ± 0.02	0.981
21	12.11	1.09 0.03	G8III	5945942146094740000	11.7453	0.62 0.01	0.976
22	12.96	0.61 0.03	F6V	5946035776383010000	12.7726	1.68 0.01	0.887
24	14.79	1.37 0.07	K1III	5945941974282210000	14.370	0.01 0.04	1.968
26	15.27	0.87 0.08	K1V	5945930154546000000	14.9807	1.32 0.03	1.028
27	14.69	0.54 0.06	F4V	5946024059712400000	14.5239	0.57 0.02	0.941

Notes.
[a] V, $B-V$ from the SMARTS 0.9 m (Subasavage et al. 2010).
[b] Spectra obtained with the RC Spectrograph on the CTIO Blanco 4 m.
[c] Parallax in mas with EDR3 errors. Modeling used uniform 1 mas error for all priors.
[d] Reduced unit weight error from EDR3.

unmodeled photocenter motion, even in the nominal "good" range of 1.0–1.4 (see also Belokurov et al. 2020). To test the effect of such tight priors, the results presented below include two separate runs of the model: the first with the original EDR3 errors, the second with uniform 1.0 mas parallax errors on those priors. Note that we utilize no parallax prior for μ Arae, an independent parallax having some value.

2. *Proper Motions:* For the reference stars we use proper-motion priors from EDR3. Simply relying on the EDR3 values for the reference stars might introduce a bias, given the limited EDR3 time span and the potentially complicated perturbations from the known components. Again, we present the two model run results below, the first including the original EDR3 proper-motion prior errors, averaging 0.02 mas yr^{-1}, the second increasing the proper-motion prior errors to 1.0 mas yr^{-1}. Again, we utilize no proper-motion priors for μ Arae.
3. *Lateral Color Corrections:* These corrections, entered into the model as data with errors, are identical to those used in Benedict & Harrison (2017).
4. *Cross-filter Corrections:* FGS 1r contains a neutral density filter, reducing the brightness of μ Arae by 5 mag (from $V = 5$ to $V = 10$), permitting us to relate the measured positions of μ Arae to far fainter reference stars all with $V > 12$. While every effort is made to build filters with plane-parallel surfaces, they are not, so some positional shift is introduced between filter-in and filter-out measures. Section 2 of Benedict et al. (2002b) describes how we derive this correction for FGS 3. Our measured values for FGS 1r were $\Delta XF_x = 8.15 \pm 0.14$ mas and $\Delta XF_y = -0.66 \pm 0.21$ mas, again, quantities introduced as observations with error in the model shown below.

3.3. Modeling the μ Arae Astrometric Reference Frame

The astrometric reference frame for μ Arae consists of six stars (Table 6). The μ Arae field (Figure 2) exhibits the distribution of astrometric reference stars (ref-20 through ref-27) used in this study. The μ Arae field was observed at a very limited range of spacecraft roll values (Table 5). Figure 3 shows the distribution in FGS 1r coordinates of the 32 sets (epochs) of μ Arae and reference star measurements. We placed μ Arae (labeled 3) in several different y locations within the FGS 1r total field of view (FOV) to maximize the number of astrometric reference stars and to ensure guide star availability for the other two FGS units. At each epoch we measured each reference star one to four times and μ Arae three to five times.

Our choice of model (Equations (3)–(4)) was driven entirely by the goodness of fit for the reference stars. We used no μ Arae observations to determine the reference frame mapping coefficients, A–F. Depending on astrometer (FGS 1r) and telescope (HST) distortions, we can solve for the following:

1. roll, offsets, and global scale (4 c, where we substitute $-B$ for D and A for E in Equation (4), with R_x, R_y removed from Equations (3)–(4));
2. roll, offsets, independent scales along each axis (6 c, Equations (3)–(4)).

By changing from 4 to 6 c, we suffer a 6% loss in degrees of freedom (dof) but obtain a 35% reduction in χ^2/dof.

3.4. The Model

From positional measurements we determine the scale, rotation, and offset "plate constants" relative to an arbitrarily adopted constraint epoch for each observation set. We employ GaussFit (Jefferys et al. 1988) to minimize χ^2. The solved equations of condition for the μ Arae field are

$$x' = x + lc_x(B - V) - \Delta XF_x \quad (1)$$

$$y' = y + lc_y(B - V) - \Delta XF_y \quad (2)$$

$$\xi = Ax' + By' + C - \mu_\alpha \Delta t - P_\alpha \varpi - \sum_{n=1}^{4} O_{n,x} \quad (3)$$

$$\eta = Dx' + Ey' + F - \mu_\delta \Delta t - P_\delta \varpi - \sum_{n=1}^{4} O_{n,y}. \quad (4)$$

Identifying terms x and y are the measured coordinates from HST, $(B - V)$ is the Johnson $(B - V)$ color of each star, lc_x and lc_y are the lateral color corrections, and ΔXF_x and ΔXF_y are cross-filter corrections applied only to μ Arae. A, B, D, and E are scale and rotation plate constants, whereas C and F are offsets; μ_α and μ_δ are proper motions; Δt is the time difference from the constraint plate epoch; P_α and P_δ are parallax factors; and ϖ is the parallax. O_x and O_y are functions of the classic orbit parameters: α, the perturbation semimajor axis; i, inclination; e, eccentricity; ω, argument of periastron; Ω, longitude of ascending node; P, orbital period; and T_0, time of periastron passage for each included component (Heintz 1978; Martioli et al. 2010). ξ and η are relative positions in R.A. and decl. that (once scale, rotation, parallax, the proper motions, and the O are determined) should not change with time.

We obtain the parallax factors from a JPL Earth orbit predictor (Standish 1990), version DE405. We obtain an orientation to the sky for the FGS 1r constraint plate (set 18 in Table 5) from ground-based astrometry (the UCAC4 Catalog) with uncertainties of $0^\circ\!.06$. At this stage we model *only* astrometry and *only* the reference stars. From histograms of the reference frame model astrometric residuals (Figure 5) we conclude that we have a well-behaved reference frame solution exhibiting residuals with Gaussian distributions with dispersions $\sigma_{(x,y)} = 1.2$ and 1.1 mas. The reference frame "catalog" from FGS 1r in ξ and η standard coordinates (Table 7) was determined with average uncertainties, $\langle \sigma_\xi \rangle = 0.70$ mas and $\langle \sigma_\eta \rangle = 0.57$ mas. Because we have rotated our constraint plate to an R.A., decl. coordinate system, ξ and η are R.A. and decl.

At this step in the analysis the astrometry knows nothing of the RV detections (Table 4). With our derived A, B, D, E, C, and F we transform the μ Arae astrometric measurements, applying A through F as constants, solving only for μ Arae proper motion and parallax, using no priors for μ Arae. Table 8 compares values for the parallax and proper motion of μ Arae from HST and Gaia (Gaia Collaboration et al. 2021). While the parallax values agree within their respective errors, we note a disagreement in the proper-motion vector ($\vec{\mu}$) absolute magnitude and direction. This could be explained by both our nonglobal proper motion measured against a small sample of reference stars and the limited duration of both astrometric studies, possibly affected by the companion perturbations. Alternatively, the mismatch between our proper motion, established through measurements taken from 2007 May to 2010 April, and the Gaia EDR3 value, a result of a campaign spanning 2014 June–2017 April, could indicate acceleration due to the companions. These differences are $\Delta\mu_{\mathrm{R.A.}} = +0.65$ mas yr^{-1} and $\Delta\mu_{\mathrm{decl.}} = +0.62$ mas yr^{-1}. Table 9 lists the proper-motion difference between our model results with weaker proper-motion priors and Gaia EDR3, showing two reference stars, ref-20 and ref-22, with differences

Table 7
Reference Star Relative Positions[a] and Measured Parallax[b]

Star	ξ	η	ϖ	RUWE
20	-24.80913 ± 0.00015	100.22019 ± 0.00014	0.28 ± 0.17	0.981
21	−115.48324 0.00010	19.89530 0.00010	1.39 0.13	0.976
22	0.65176 0.00012	76.26965 0.00010	1.73 0.13	0.887
24	−66.90436 0.00021	18.47734 0.00018	−0.77 0.23	1.968
26	57.26613 0.00021	−74.94361 0.00020	1.28 0.21	1.028
27	116.18275 0.00018	61.11125 0.00016	0.76 0.19	0.941

Notes.
[a] Units are arcseconds, rolled to R.A. (ξ) and decl. (η), epoch 2008.6524 (J2000). Roll uncertainty $\pm0\overset{\circ}{.}02$.
[b] Final values from a model with input parallax prior errors 1 mas and input proper-motion priors 1 mas yr^{-1}.
[c] R.A. = 266.0392504, decl. = −51.8140955, J2000.

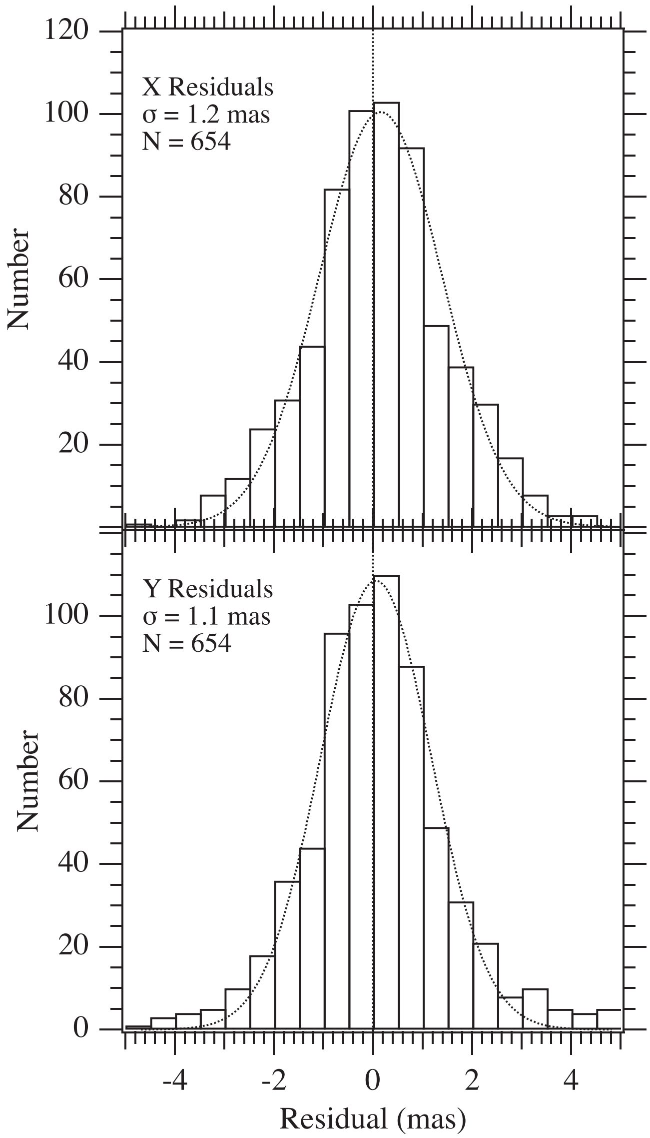

Figure 5. Histograms of x and y residuals obtained by deriving the coefficients of Equations (2)–(5) from 654 reference star measures, while modeling reference star parallax and proper motion. The priors for this model had the published EDR3 errors. Distributions are fit with Gaussians, with standard deviations, σ, indicated in each panel.

almost as large as those for μ Arae. Furthermore, Brandt (2021) finds a low χ^2 value when solving a model assuming no proper-motion change, comparing Hipparcos with Gaia, indicating little to no μ Arae acceleration over a roughly 25 yr time span.

Table 8
Reference Frame Statistics, μ Arae Parallax, and Proper Motion

Parameter	Value
Study duration	2.85 yr
Number of observation sets	32
Reference star $\langle V \rangle$	13.67
Reference star $\langle (B-V) \rangle$	1.00
HST: model with reference star EDR3 prior errors	
Absolute ϖ	63.84 ± 0.13 mas
Relative μ_α	-14.44 ± 0.13 mas yr^{-1}
Relative μ_δ	-190.25 ± 0.12 mas yr^{-1}
$\vec{\mu} = 190.79$ mas yr^{-1}	
P.A.=$184\overset{\circ}{.}3$	
HST: model with reference star EDR3 1 mas and 1 mas^{-1} prior errors	
Absolute ϖ	64.11 ± 0.13 mas
Relative μ_α	-14.38 ± 0.13 mas yr^{-1}
Relative μ_δ	-190.28 ± 0.12 mas yr^{-1}
$\vec{\mu} = 190.83$ mas yr^{-1}	
P.A.=$184\overset{\circ}{.}3$	
Gaia EDR3 Absolute ϖ	64.09 ± 0.09 mas
Absolute μ_α	-15.03 ± 0.08 mas yr^{-1}
Absolute μ_δ	-190.90 ± 0.07 mas yr^{-1}
$\vec{\mu} = 191.49$ mas yr^{-1}	
P.A.=$184\overset{\circ}{.}5$	

4. Astrometric Detection Limits for μ Arae Companions

We included μ Arae in our original HST proposal based on an expected perturbation ($2 \times \alpha$) for each minimum-mass ($\mathcal{M}$ sin i) companion, obtained through pert $= 0.2(P^{2/3}\mathcal{M}_p) / ((d/10) \times \mathcal{M}_*^{2/3})$ mas, with P the companion period, $\mathcal{M}_p$ the known $\mathcal{M}$ sin i, d the distance in pc, and $\mathcal{M}_*$ the mass of μ Arae. The then known minimum masses (little changed by our Table 4 improved orbits) were $\mathcal{M}$ sin i b, c, d, e = 1.7, 0.03, 0.52, 1.81 $\mathcal{M}_{\rm Jup}$, yielding minimum perturbation sizes 0.28, 0.0003, 0.05, 0.99 mas. Clearly, FGS astrometry had no hope of detecting μ Arae c, but the HST Time Allocation Committee agreed that it was worth a shot for at least two of the other components, b and e. As previously mentioned, the reference frame solution exhibited residual Gaussian distributions with dispersions $\sigma_{(x,y)} = 1.2$ and 1.1 mas. The μ Arae residuals have $\sigma_{(x,y)} = 1.7$ and 1.5 mas, possibly signaling unmodeled motion. These residuals should now

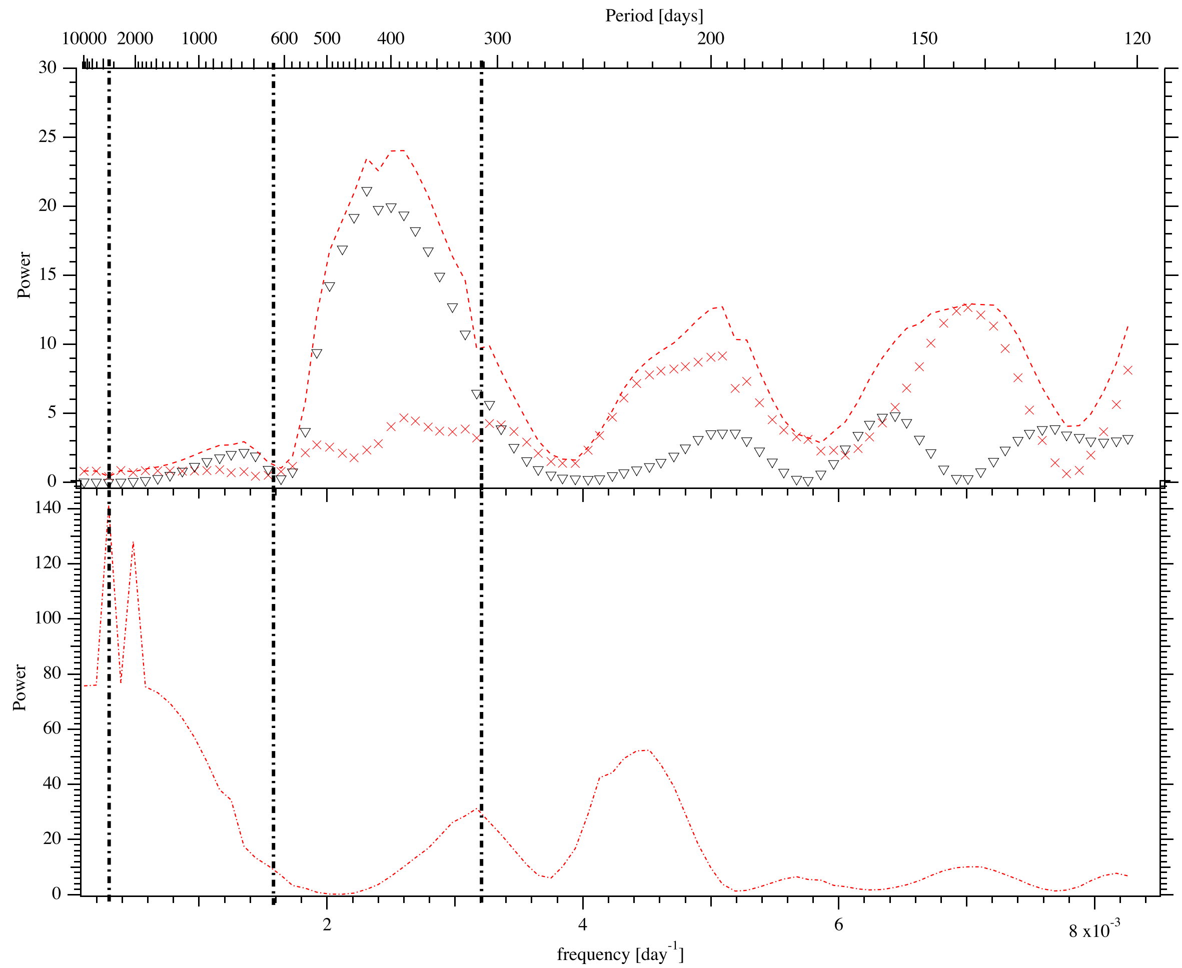

Figure 6. Normalized Lomb–Scargle periodograms (Zechmeister & Kürster 2009) of μ Arae astrometry residuals obtained by applying the coefficients of Equations (2)–(5) to μ Arae, solving only for μ Arae proper motion and parallax (top), and the window function for the μ Arae observation sequence (bottom). Vertical lines indicate RV-determined periods for (left to right) components e, b, and d. We find no significant power in the residuals at any component period.

Table 9
Reference Star Proper Motions[a] and Agreement with EDR3[b]

Star #	$\mu_{\rm R.A.}$	$\mu_{\rm Decl.}$	$\Delta\mu_{\rm R.A.}$	$\Delta\mu_{\rm Decl.}$
20	−3.06 ± 0.19	−2.91 ± 0.16	−0.53	0.14
21	2.38 0.12	0.21 0.12	0.02	0.01
22	0.79 0.14	−16.63 0.12	0.42	−0.33
24	−5.31 0.24	−5.85 0.21	0.11	0.06
26	−18.52 0.22	−17.55 0.20	−0.11	−0.02
27	1.99 0.21	−2.88 0.18	0.06	0.08

Notes.
[a] Units: mas yr^{-1}.
[b] Difference from a model with input parallax prior errors 1 mas and input proper-motion priors 1 mas yr^{-1}.

contain only measurement noise, possible systematic effects, and perturbations due to suspected companions, μ Arae b, c, d, and e.

We now have access to other predictive resources. These include the Gaia EDR3 RUWE parameter, which predicts unmodeled photocenter motion (Stassun & Torres 2021), and the Brandt (2021) χ^2 value. The latter parameter measures an amount of measured acceleration obtained by comparing an earlier-epoch proper motion from Hipparcos with an EDR3 proper motion. A larger χ^2 value indicates more significant change (acceleration) in proper motion and thus a higher probability of a perturbing companion. Table 11 lists results from all past FGS exoplanet astrometry, carried out to establish companion masses. For each result we tabulate RUWE and degree of likely acceleration, given by the χ^2 value. The entries are sorted by RUWE value, highest to lowest, more potential unmodeled (by Gaia) image motion to less. Note that the subject of this study, μ Arae, sits at the bottom. Neither RUWE nor the relatively low χ^2 value predicts ease of companion detection. Higher values might be caused by the still experimental Gaia centroiding for bright stars. To test this possibility, we sampled 24 stars, $3.6 < G < 7$, within 4° of μ Arae. This sample had median RUWE, χ^2 values of 1.0 and 5.4, giving μ Arae, with 0.86 and 2.35, a low probability of companion detectability. Note that γ Cep AB is a long-period binary star system, hence the very large χ^2 value.

Forging ahead, despite the gloomy outlook, we subject those μ Arae astrometric residuals to the following test. In Figure 6 we compare Lomb–Scargle periodograms of astrometric residuals generated before allowing ($O_{n,x}$) and ($O_{n,y}$) to reduce residuals. A periodogram of μ Arae residuals to a model without orbital motion (Figure 6, top) contains no significant companion signatures at periods indicated by the RV analysis (Table 4).

What could "hide" in astrometry with per-observation precision a little over 1 mas as demonstrated in Figure 5? We

Table 10
Component Mass Upper Limits

Component	P (yr)	α (mas)[a]	$\mathcal{M}(\mathcal{M}_{\rm Jup})$
b	1.8	0.35	4.3
d	0.8	0.35	7.0
e	10.9	1.20	4.4

Note.
[a] Detectable perturbation size given reference frame noise levels.

estimate mass upper limits for the known companions by first populating the μ Arae observation dates with Gaussian noise having levels corresponding to the reference star model results in Figure 5, $\sigma_{\rm x,y} = 1.2$ and 1.1 mas. Working with each known companion, μ Arae b, d, e, separately, we add orbital motion, generating signals with various perturbation amplitudes, α, using the RV orbital elements from Table 4, holding the unknown longitude of ascending node, $\Omega = 0°$, and the unknown inclination, $i = 0°$. For each α we inspect the periodogram for a signal near the component b, d, e period. An α producing a signal with a false-positive level less than 1% becomes our presumed detection limit, a perturbation we should have seen, given the measured noise level in our astrometry. We then assume a μ Arae mass of 1.13 $\mathcal{M}_\odot$, which, with the known period, provides a companion mass. We provide these mass upper limits in Table 10 and associated periodograms in Figure 7. Assuming an expected inclination, $i = 60°$ (see Section 5.1 for the source of this expectation), increases the mass limits by approximately 50%.

Our measurement precision and extended study duration have improved the accuracy of the parallax of μ Arae.

5. Exoplanets with the FGS

Given that μ Arae is the final (and only null) result from our originally proposed HST FGS investigations, we now investigate one aspect of that astrometry. Our past exoplanet mass determinations (Table 3; Benedict et al. 2017; Benedict & Harrison 2017; Benedict et al. 2018; Benedict & McArthur 2020) all critically depend on the inclinations we obtain from our astrometry. These inclinations are listed in Table 11, along with perturbation semimajor axis and the two parameters that can signal deviations from a model solving only for proper motion and parallax.

5.1. Evidence for Inclination Bias

Table 11 suggests that our exoplanet orbit inclinations seem to skew to small values. Is there some insidious systematic error in all our analyses that would result in our recovering overly small inclinations, with the result that we find systems to be more face-on than their true orientation?

We test that our exoplanet perturbation inclinations may not be random by first obtaining a sample of measured inclinations with an assumed random distribution. We harvest over 3200 measured inclinations from the 6th Catalog of Visual Binary Stars (Washington Double Star (WDS); Hartkopf et al. 2001) and produce the cumulative distribution function (CDF) displayed in Figure 8. To produce the CDF, we put all inclinations on a 0°–90° scale by applying this offset to any inclinations over 90°; $i_{\rm corr} = 90° - {\rm mod}(i, 90°)$. A histogram of these inclinations exhibits a peak at $i_{\rm corr} = 60°$, as expected from a sample of random orientations. Also plotted are the CDF for the (Benedict et al. 2016, Table 9) visual binary inclinations (HST Binaries, offset as above) and the CDF for the exoplanetary perturbations listed in Table 11 (ExoP).

To assess the probability that two CDFs are both drawn from random distributions, we employ a Kolmogorov–Smirnov (K-S) test, which produces a test statistic, D, a critical value, C, and a p value, PV. Values of D less than C support the null hypothesis. A p-value greater than the adopted significance level (all $\alpha = 0.05$) also supports the null hypothesis. Table 12 summarizes the results of K-S tests to support or refute the null hypothesis that two distributions (first MLR binary inclinations, then exoplanet inclinations) are drawn from the same parent population (randomly distributed inclinations).

First, because the Benedict et al. (2016) low-mass mass–luminosity relation (MLR) binary system inclinations do contain a bias toward lower inclinations (those systems being more favorable for discovery, and for the subsequent astrometric measurement required to establish precise stellar masses), as expected, the null hypothesis that HST MLR inclinations are as random as the 6th Catalog inclinations is not supported, D is marginally larger than C, and the p-value is lower than the significance level, α (Table 12). Second, Figure 8 shows an exoplanet inclination CDF strikingly dissimilar to the random inclination CDF from the WDS catalog. K-S testing the Table 11 exoplanet inclinations against the known random 6th Catalog inclinations, we find D greatly exceeding C and p much lower than α (Table 12). Our HST astrometrically derived exoplanet orbit inclinations are clearly inconsistent with a sample with a random distribution of inclinations.

5.2. Possible Bias Explanations

We now explore four potential areas that could produce the observed bias in our exoplanet system inclinations: small number statistics, modeling technique, FGS mechanical issues, and orbit modeling of noise-dominated data. None of them adequately explain the clearly demonstrated bias.

5.2.1 Small Number of Inclinations

To explore any possible effect of comparing unequal sampling sizes, we drew from the 6th Catalog 100,000 randomly selected samples of inclination, each with 12 values representing the exoplanet sample. Running K-S tests comparing each sample CDF with the 6th Catalog CDF, we find only a 5% probability of a randomly selected sample CDF disagreeing with the 6th Catalog. This Monte Carlo test suggests that small number statistics are highly unlikely to be the cause of the exoplanet inclination bias.

5.2.2 Restricted Modeling

Hipparcos intermediate astrometric data (IAD) have been used in several studies to estimate the mass or upper mass limits for possible exoplanets (e.g., Mazeh et al. 1999; Reffert & Quirrenbach 2011). Pourbaix (2001) found that some small inclinations were merely artifacts of the fitting procedure that was used. Fitting (i, Ω) to the HIP IAD, where the $\alpha \sin i$ is much smaller than the astrometric precision, always yields low values of $\sin i$, regardless of the true inclination.

For our analysis we force astrometry and RV to describe the same perturbations through this constraint (e.g., Pourbaix &

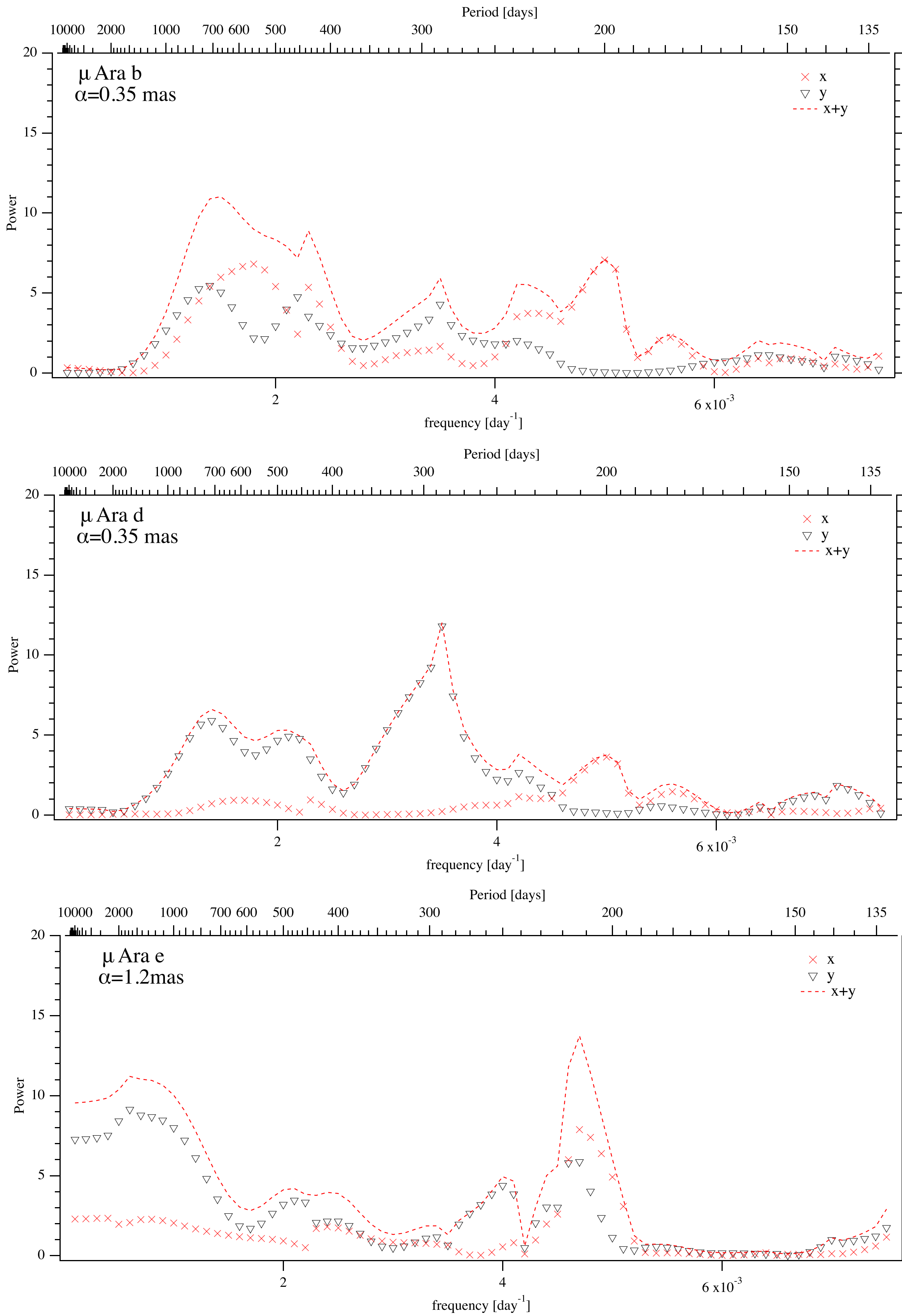

Figure 7. Estimated detection thresholds using Lomb–Scargle periodograms for each component, with perturbation amplitude indicated. A power level of 10 yields a false-positive level of 1%.

Table 11
HST Exoplanet Perturbations and Inclinations

ID	α (mas)	i (deg)	i_{corr}[a] (deg)	RUWE[b]	χ^2 [c]	Source
υ And d	1.39 ± 0.07	23.8 ± 1.3	23.8	7.25	6.39	1
υ And c	0.62 0.08	7.9 1	7.9	…	…	1
γ Cep Ab	1.1 0.1	169.5 1.1	10.5	3.21	4771	2
ϵ Eri b	1.88 0.2	45 8	30.1	2.72	33.89	3
HD 33636 A	5 0.2	14 0.1	14	1.88	55.6	4
HD 136118 b	1.45 0.25	163.1 3	16.9	1.43	71.32	5
GJ 876 b	0.25 0.06	84 6	84	1.34	3.56	6
HD 128311 c	0.46 0.09	56 15	56	1.31	12.64	7
HD 38529 c	1.05 0.06	48.3 3.7	48.3	1.05	5.3	8
HD 202206c	0.76 0.11	7.7 1.1	7.7	1.03	32.25	9
Prox Cen c	0.5 0.1	18 4	18	0.97	0.51	10
55 Cnc d	1.9 0.4	53 7	53	0.86	1.81	11
μ Arae				0.86	2.35	

Notes.
[a] $i_{corr} = 90° - \mathrm{mod}(i, 90°)$ for $i > 90°$.
[b] RUWE, reduced unit weight error from Gaia EDR3. Larger RUWE implies photocenter motion in excess of measured parallax and proper motion.
[c] A larger χ^2 value indicates more significant acceleration in proper motion (Brandt 2021) and thus a higher probability of a perturbing companion.
References. 1 = McArthur et al. (2010); 2 = Benedict et al. (2018); 3 = Benedict (2022); 4 = Bean et al. (2007); 5 = Martioli et al. (2010); 6 = Benedict et al. (2002a); 7 = McArthur et al. (2014); 8 = Benedict et al. (2010); 9 = Benedict & Harrison (2017); 10 = Benedict & McArthur (2020); 11 = McArthur et al. (2004).

Jorissen 2000), shown for a perturbing companion b:

$$\frac{\alpha_b \sin i_b}{\varpi_{abs}} = \frac{P_b K_b (1 - e_b^2)^{1/2}}{2\pi \times 4.7405}. \quad (5)$$

Equation (5) contains quantities derived from astrometry (parallax, ϖ_{abs}, host star perturbation orbit size, α, and inclination, i) on the left-hand side (LHS) and quantities derivable from both the period P and eccentricity ϵ, or only RVs (the RV amplitude of the primary, K, induced by a companion), on the right-hand side (RHS). HST time is in high demand. This, in most cases, results in sparse orbit coverage of any perturbation afforded by the astrometry. Therefore, the RV data were always essential in determining a perturbation orbit. For a multicomponent system, $n = 1$, 2, 4 (for example, μ Arae b, d, e), $O_{n,x}$ and $O_{n,y}$ in Equations (3) and (4) are functions of the classic orbit parameters. They describe the motion (on the sky and in RV) of the parent star around the barycenter. The RVs cover a far greater time span for each component perturbation, providing essential support for determining P, ϵ, K, ω, and T_0.

While for our analysis we do use a relationship between the astrometry and the RV (see Equation (5)), our modeling is significantly different than the modeling of the HIP IAD. We hold no orbital or astrometric parameters as constants. Our solutions do not converge unless there is a measurable signal. Given the relatively short time span for the astrometric measures, our past and present analyses critically depend on both RV measures secured over longer time spans and the Equation (5) relation between astrometry (LHS) and RV (RHS). For most of the targets in Table 11 the period, amplitude, and eccentricities from RV only are well determined, with errors insufficient to much change the LHS inclination via Equation (5). To increase the inclination requires a decrease in either parallax or perturbation size, or both.

5.2.3 FGS at Fault

We now estimate possible errors for our parallax and perturbations, using HD 202206c as a test case (Benedict & Harrison 2017). Figure 9 compares a subset of FGS parallaxes (Benedict et al. 2017, Table 1) with Gaia EDR3 (Lindegren et al. 2021b), where the subset satisfies Gaia RUWE < 1.4. Based on the EDR3 error assessments of Stassun & Torres (2021) and Lindegren et al. (2021a), we assume that Gaia parallaxes are error-free, a reasonable assumption given the ∼0.03 mas errors compared to the average ∼0.19 mas errors for HST. Figure 9 yields FGS parallax errors typically less than 1 mas, assuming Gaia perfection. Holding all other terms in Equation (5) constant, to increase the astrometric inclination for HD 202206c from the measured 7° to, for example, 40° would require a parallax $\varpi = 105$ mas (the Benedict & Harrison 2017 value is 21.96 mas), a parallax mismeasurement far exceeding what we have achieved in the past. This leaves only the perturbation size, α, suspect.

All FGS parallax measurements have built-in constraints similar to those we employ to derive an exoplanet perturbation, α. The precisely known period and eccentricity of the orbit of Earth serve as the RHS terms of Equation (5). The calculated parallax factors encode those terms plus a perceived inclination, basically the ecliptic latitude of the parallax target. As demonstrated in Figure 9, our errors in determining the parallactic ellipse size rarely exceed 1 mas. The majority of those results came from campaigns with $N = 9$–11 measurement sets (e.g., Benedict et al. 2007). Astrometric accuracy scales as $1/\sqrt{N}$. Thus, with 31 observational epochs we might realistically expect errors in HD 202206 α and ϖ of ∼0.5 mas. Increasing the inclination to 40° would decrease the HD 202206 perturbation to $\alpha = 0.16$ mas. To yield the average inclination expected by the assumption that orbit angular momentum vectors for exoplanet systems are randomly and isotropically distributed (60°) would require $\alpha = 0.12$ mas, an unlikely 6σ difference.

Our Monte Carlo tests show how unlikely it is that we, by chance, studied many exoplanetary systems with

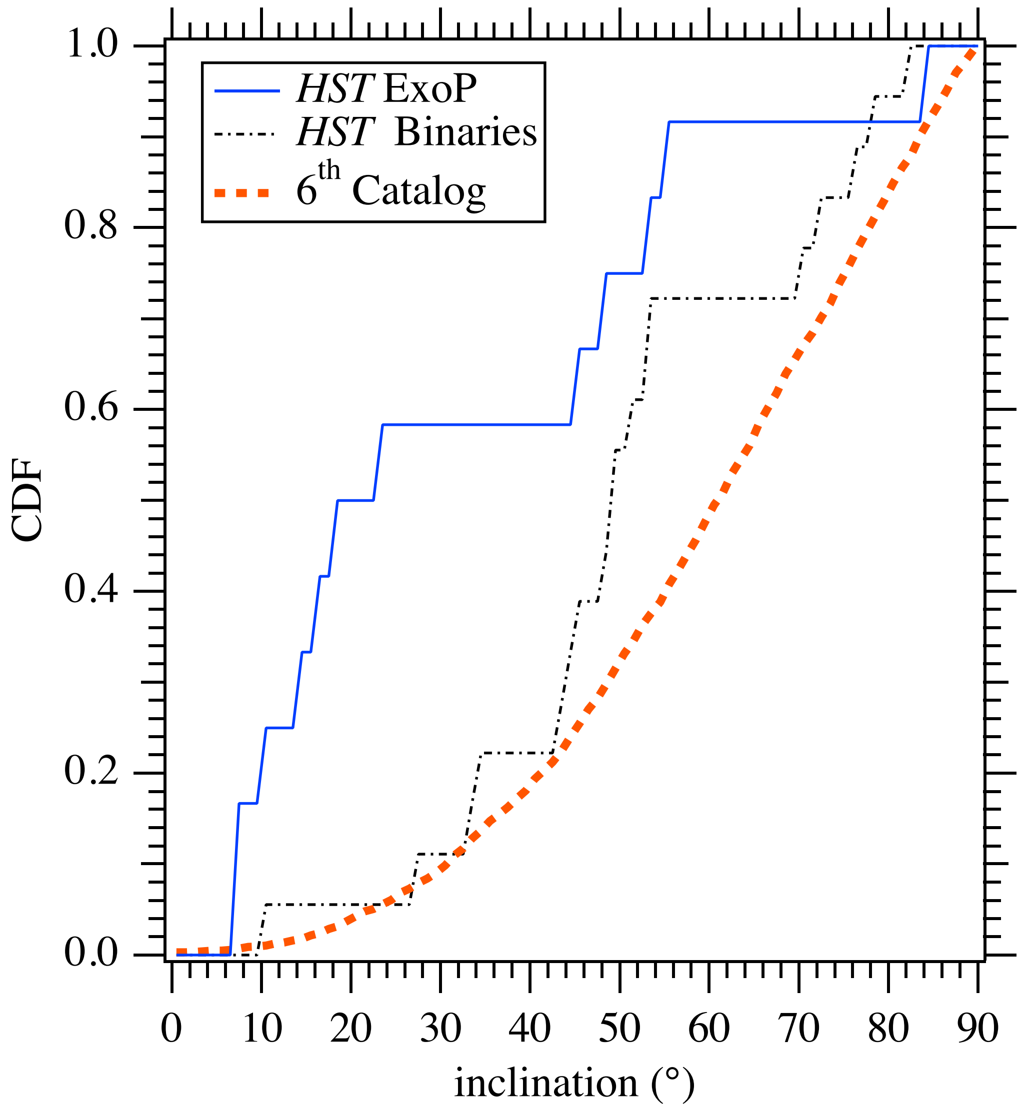

Figure 8. CDFs for the entire inclination set from the 6th Visual Binary Star Catalog (WDS), inclinations for HST-measured binary stars from Benedict et al. (2016), and exoplanet perturbation inclinations (Table 11). K-S test results (Table 12) indicate that neither our exoplanet inclination distributions nor the HST binary distributions are drawn from the same parent population as the 6th Catalog binary inclination population.

Table 12
K-S Test Results

Test	D	C	α	p
HST MLR versus 6th Catalog	0.35	0.34	0.050	0.02
ExoP versus 6th Catalog	0.53	0.41	0.050	0.00

lower-than-expected inclinations. However, two recent results argue for small number statistics rather than systematic bias. These systems also yield low inclinations. The first is (Benedict & McArthur 2020) Proxima Centauri c, with an inclination $i_c = 18° \pm 4°$, which, modulo 90°, agrees with Kervella et al. (2020). The second is vA 351, a complex binary in the Hyades, consisting of components AD and BC with a 2.7 yr orbital period, and components BC in a 0.75-day orbital period (Benedict et al. 2021). FGS fringe tracking, fringe scanning, and independent speckle camera observations yield an AD–BC inclination $i = 14° \pm 8°$. Extensive RV measurements yield a mass ratio for components B/C. That ratio, coupled with a total BC mass from FGS astrometry, yields masses for the B and C components that agree within 7% with those predicted from the Benedict et al. (2016) MLR, further confirming the validity of our measured system inclination.

5.2.4 Fitting an Orbit to Astrometric Noise

For this test we choose κ Pavonis, a dwarf Cepheid, previously a parallax target (Benedict et al. 2011; parallax $\varpi = 5.57 \pm 0.28$ mas). The modeling resulted in a $\chi^2/\mathrm{dof} = 0.426$ and an rms residual of 1.9 mas. This parallax agrees within the errors with the Gaia EDR3 value, $\varpi = 5.24 \pm 0.12$ mas. For κ Pav, RUWE = 2.29, a high value likely due to photometric variability and brightness ($G < 6$), there yet being no astrometric, RV, or direct imaging evidence of a companion. The Brandt (2021) $\chi^2 = 6.58$ is close to the median value, 5.4, found for a random sample of similarly bright stars (Section 4). We modified the model to solve for an orbit, including totally fictitious priors for period $P = 435 \pm 3$ days, eccentricity $e = 0.3 \pm 0.1$, time of periastron passage $T_0 = 53{,}041 \pm 30$ days, longitude of periastron passage $\omega = 269° \pm 17°$, and RV amplitude $K = 113 \pm 20$ m s^{-1}. This

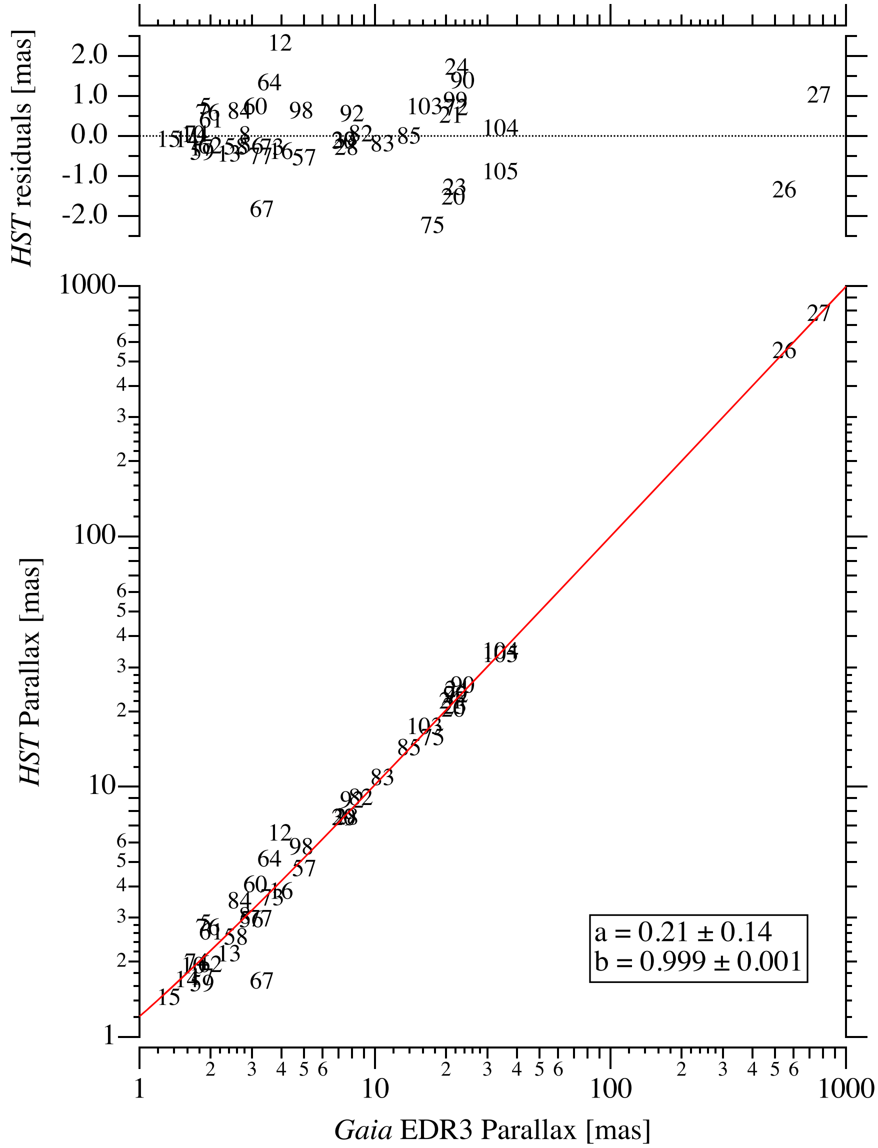

Figure 9. HST FGS parallaxes compared with Gaia EDR3 parallaxes. The linear regression assumes no errors for Gaia. Comparison plots only targets with Gaia RUWE < 1.4, ID numbers from Table 1 in Benedict et al. (2017): 5, 8, 10, 12, 13, 14, 15, 16, 17, 20, 21, 23, 24, 26, 27, 28, 29, 30, 56, 57, 58, 59, 60, 61, 62, 64, 67, 72, 73, 74, 75, 76, 77, 82, 83, 84, 85, 90, 92, 98, 99, 103, 104, and 105. The HST residuals have an rms value 0.82 mas.

produces an orbit with a perturbation size $\alpha = 0.4 \pm 0.2$ mas and an inclination $i = 2\overset{\circ}{.}9 \pm 1\overset{\circ}{.}5$. The $\chi^2/\mathrm{dof} = 0.417$ is only 2% less than a model without the orbit. The rms residual is unchanged at 1.9 mas. While including an orbit did produce a result with a very small decrease in χ^2/dof, we find no effect on the rms residual. That and the very low statistical significance of the α and inclination values (2σ) demonstrate a companion nondetection. Our previous inclination and perturbation results (Table 11) are all $> 5\sigma$, demonstrably not a result of fitting noise.

6. System Stability

μ Arae has always presented stability challenges (Pepe et al. 2007; Timpe et al. 2013; Laskar & Petit 2017; Agnew et al. 2018). Our remodeling of a larger set of RV supports the conclusion of Timpe et al. (2013) that μ Arae b and d are *near* a 2:1 resonance; $P_\mathrm{b}/P_\mathrm{d} = 2.095 \pm 0.002$. Our improved period for the outermost companion, e, places it *near* a 6:1 resonance with component b, $P_\mathrm{e}/P_\mathrm{b} = 6.12 \pm 0.04$. Note that Laskar & Petit (2017) include μ Arae (and the solar system) among the unstable systems.

However, our incomplete characterization of the μ Arae system (minimum masses from Section 4) fails to provide a solution to the vexing problem of stability. The orbital periods are similar to those of Earth, Mars, and Jupiter, but of course the masses are much larger. These features suggest that gravitational interactions should induce large-amplitude oscillations in the orbital elements, potentially resulting in ejections or collisions between the orbiting bodies. Here we examine these interactions with analytic and *N*-body methods. We find that the results inferred from the astrometric and RV observations predict an unstable system.

We first consider the Hill stability (Szebehely & Zare 1977; Marchal & Bozis 1982; Gladman 1993) of the three planet–planet pairs to assess the likelihood of orbital stability. Hill stability is only strictly applicable to a three-body system outside of resonance, but it is analytic and can provide an approximate assessment of stability in more complicated systems such as μ Arae. Following the prescription of Barnes & Greenberg (2006, 2007), we characterize the Hill stability via the ratio $\beta/\beta_{\rm crit}$ in which ratios less than 1 indicate instability and ratios greater than 1 indicate stability. We use the publicly available code `HillStability`[7] to calculate this value and find that the b–d pair is at the limit with $\beta/\beta_{\rm crit} = 1.0$. The other pairs appear comfortably stable.

We support this prediction with a direct *N*-body simulation. We integrated our best-fit system with the `SpiNBody` module in `VPLanet` (Barnes et al. 2020)[8] to model evolution from first principles. We used a fixed time step of 0.365 days corresponding to nearly 1000 steps per orbit for planet d with `VPLanet`'s fourth-order Runge–Kutta scheme, which is generally small enough to capture the evolution. We find that the system breaks apart owing to interactions between planets b and d in less than 10^5 yr, confirming the instability predicted by the Hill theory.

Thus, μ Arae continues to be problematic in terms of orbital stability, but our Hill stability analysis suggests that modest changes to the system, particularly the masses and orbits of planets b and d, could result in a stable system. Alternatively, we find that if we remove planet d from the system, then the resulting orbital evolution is regular and long-term stability appears likely.

7. Summary

For the μ Arae system, from a model that utilizes HST FGS astrometry and ground-based RV we find the following:

1. Significantly improved companion orbital elements (P, ϵ, ω, T_0, K), derived from only the large body of RV data.
2. With a model containing no proper-motion and parallax priors for μ Arae a parallax $\pi_{\rm abs} = 64.11 \pm 0.13$ mas, agreeing with the Hipparcos and Gaia EDR3 values within the errors, and a proper motion relative to a Gaia EDR3 reference frame, $\boldsymbol{\mu} = 190.83$ mas yr^{-1}, with a position angle P.A. = 184°.3, differing by +0.66 mas yr^{-1} and − 0°.2 compared to Gaia EDR3.
3. That astrometric residuals of order 1 mas to models solving only for parallax and proper motion contain no evidence for any of the known companions of μ Arae.
4. Assuming those levels of measurement precision yields lower limits for μ Arae b, d, e of 4.3, 7.0, and 4.4 $\mathcal{M}_{\rm Jup}$.
5. That K-S testing supports the assertion that exoplanetary orbit inclinations previously measured with the HST FGS are biased toward small inclinations. Based on comparisons with Gaia EDR3 parallaxes, the results from an orbit determination when none exists, and independently confirmed recent results, we argue that this could be chance, not systematic error.
6. An inherently unstable system, if it includes μ Arae d.
7. A system stable for 10^6 yr without μ Arae d.

Finally, all HST FGS exoplanet results represent a useful test of Gaia results. With 10–100 μas precision and a longer time span for astrometric observations, Gaia will certainly improve on those results, either exposing a bias in FGS exoplanet astrometry or not. If HST FGS exoplanet results do contain a bias, then Gaia investigators, who will produce a large number of perturbation orbital elements with perturbations near the Gaia per-observation precision, should be aware of this possibility. We hope that a future combination of FGS and RV data with Gaia can improve the accuracy of any astrometric result and definitively produce companion orbits and masses.

We thank Dr. Tim Brandt for the careful, well-reasoned referee's report, which significantly improved the paper content, and an initial anonymous referee for flag raising. This work is based on observations made with the NASA/ESA Hubble Space Telescope, obtained at the Space Telescope Science Institute. Support for this work was provided by NASA through grants 11210 and 11788 from the Space Telescope Science Institute, which is operated by the Association of Universities for Research in Astronomy, Inc., under NASA contract NAS5-26555. R.B. acknowledges support from the NASA Astrobiology Program grant No. 80NSSC18K0829. This publication makes use of data products from the Two Micron All Sky Survey, which is a joint project of the University of Massachusetts and the Infrared Processing and Analysis Center/California Institute of Technology, funded by NASA and the NSF. This research has made use of the SIMBAD and Vizier databases, operated at Centre Donnees Stellaires, Strasbourg, France; Aladin, developed and maintained at CDS; the NASA/IPAC Extragalactic Database (NED), which is operated by JPL, California Institute of Technology, under contract with NASA; and NASA's truly essential Astrophysics Data System Abstract Service. This work has made use of data from the European Space Agency (ESA) mission Gaia (http://www.cosmos.esa.int/gaia), processed by the Gaia Data Processing and Analysis Consortium (DPAC, http://www.cosmos.esa.int/web/gaia/dpac/consortium). Funding for the DPAC has been provided by national institutions, in particular the institutions participating in the Gaia Multilateral Agreement. Many people over the years have materially improved all aspects of the work reported, particularly Linda Abramowicz-Reed, Art Bradley, Denise Taylor, and all the coauthors of our many papers. We thank Dr. Paul Robertson for use of his code based on the Zechmeister and Kürster normalized Lomb–Scargle algorithm. The American Astronomical Society supported the preparation of this paper while G.F.B. carried out duties as Society Secretary, and is sincerely grateful for this (and publication support). G.F.B. fondly remembers Debbie Winegarten (R.I.P.), whose able assistance with secretarial matters freed him to devote time to this analysis.

ORCID iDs

G. F. Benedict https://orcid.org/0000-0003-2852-3279
E. P. Nelan https://orcid.org/0000-0002-5704-5221
R. Wittenmyer https://orcid.org/0000-0001-9957-9304
R. Barnes https://orcid.org/0000-0001-6487-5445
H. Smotherman https://orcid.org/0000-0002-7895-4344
J. Horner https://orcid.org/0000-0002-1160-7970

References

Agnew, M. T., Maddison, S. T., & Horner, J. 2018, MNRAS, 481, 4680
Barnes, R., & Greenberg, R. 2006, ApJL, 647, L163
Barnes, R., & Greenberg, R. 2007, ApJL, 665, L67
Barnes, R., Luger, R., Deitrick, R., et al. 2020, PASP, 132, 024502
Bean, J. L., McArthur, B. E., Benedict, G. F., et al. 2007, AJ, 134, 749
Belokurov, V., Penoyre, Z., Oh, S., et al. 2020, MNRAS, 496, 1922
Benedict, G. 2007, HST Proposal ID 11210
Benedict, G. F. 2022, RNAAS, 6, 45

[7] https://github.com/RoryBarnes/HillStability
[8] `VPLanet` is publicly available at https://github.com/VirtualPlanetaryLaboratory/vplanet.

Benedict, G. F., Franz, O. G., Horch, E. P., et al. 2021, AJ, 161, 285
Benedict, G. F., & Harrison, T. E. 2017, AJ, 153, 258
Benedict, G. F., Harrison, T. E., Endl, M., et al. 2018, RNAAS, 2, 7
Benedict, G. F., Henry, T. J., Franz, O. G., et al. 2016, AJ, 152, 141
Benedict, G. F., & McArthur, B. E. 2020, RNAAS, 4, 86
Benedict, G. F., McArthur, B. E., Bean, J. L., et al. 2010, AJ, 139, 1844
Benedict, G. F., McArthur, B. E., Feast, M. W., et al. 2007, AJ, 133, 1810
Benedict, G. F., McArthur, B. E., Feast, M. W., et al. 2011, AJ, 142, 187
Benedict, G. F., McArthur, B. E., Forveille, T., et al. 2002a, ApJL, 581, L115
Benedict, G. F., McArthur, B. E., Franz, O. G., et al. 2001, AJ, 121, 1607
Benedict, G. F., McArthur, B. E., Fredrick, L. W., et al. 2002b, AJ, 123, 473
Benedict, G. F., McArthur, B. E., & Harrison, T. E. 2018, RNAAS, 2, 22
Benedict, G. F., McArthur, B. E., Nelan, E. P., et al. 2017, PASP, 129, 012001
Bonfanti, A., Ortolani, S., Piotto, G., et al. 2015, A&A, 575, A18
Brandt, T. D. 2021, ApJS, 254, 42
Butler, R. P., Tinney, C. G., Marcy, G. W., et al. 2001, ApJ, 555, 410
Díaz, M. R., Jenkins, J. S., Tuomi, M., et al. 2018, AJ, 155, 126
Diego, F., Charalambous, A., Fish, A. C., et al. 1990, Proc. SPIE, 1235, 562
Feng, F., Tuomi, M., & Jones, H. R. A. 2017, MNRAS, 470, 4794
Fischer, D. A., & Valenti, J. 2005, ApJ, 622, 1102
Ford, E. B. 2006, in ASP Conf. Ser. 352, What Do Multiple Planet Systems Teach Us about Planet Formation? (San Francisco, CA: ASP), 15
Gaia Collaboration, Brown, A. G. A., Vallenari, A., et al. 2021, A&A, 649, A1
Gladman, B. 1993, Icar, 106, 247
Gould, A., & Morgan, C. W. 2003, ApJ, 585, 1056
Harrison, T. E., McNamara, B. J., Szkody, P., et al. 1999, ApJL, 515, L93
Hartkopf, W. I., Mason, B. D., & Worley, C. E. 2001, AJ, 122, 3472
Heintz, W. D. 1978, Double Stars. D (Dordrecht: Reidel)
Jefferys, W. H., Fitzpatrick, M. J., & McArthur, B. E. 1988, CeMec, 41, 39
Kervella, P., Arenou, F., & Schneider, J. 2020, A&A, 635, L14
Laskar, J., & Petit, A. C. 2017, A&A, 605, A72
Lindegren, L., Bastian, U., Biermann, M., et al. 2021a, A&A, 649, A4
Lindegren, L., Klioner, S. A., Hernández, J., et al. 2021b, A&A, 649, A2
Lo Curto, G., Pepe, F., Avila, G., et al. 2015, Msngr, 162, 9
Marchal, C., & Bozis, G. 1982, CeMec, 26, 311
Martioli, E., McArthur, B. E., Benedict, G. F., et al. 2010, ApJ, 708, 625
Mazeh, T., Zucker, S., Dalla Torre, A., et al. 1999, ApJL, 522, L149
McArthur, B. E., Benedict, G. F., Barnes, R., et al. 2010, ApJ, 715, 1203
McArthur, B. E., Benedict, G. F., Harrison, T. E., et al. 2011, AJ, 141, 172
McArthur, B. E., Benedict, G. F., Henry, G. W., et al. 2014, ApJ, 795, 41
McArthur, B. E., Benedict, G. F., Jefferys, W. J., & Nelan, E. 2006, in The 2005 HST Calibration Workshop: Hubble After the Transition to Two-Gyro Mode, ed. A. M. Koekemoer, P. Goudfrooij, & L. L. Dressel (Washington, DC: NASA), 396
McArthur, B. E., Endl, M., Cochran, W. D., et al. 2004, ApJL, 614, L81
Nelan, E. 2015, FGS Instrument Handbook (Baltimore, MD: STScI)
Pepe, F., Correia, A. C. M., Mayor, M., et al. 2007, A&A, 462, 769
Pourbaix, D. 2001, A&A, 369, L22
Pourbaix, D., & Jorissen, A. 2000, A&AS, 145, 161
Rajpaul, V., Aigrain, S., & Roberts, S. 2016, MNRAS, 456, L6
Reffert, S., & Quirrenbach, A. 2011, A&A, 527, A140
Robertson, P., Mahadevan, S., Endl, M., et al. 2014, Sci, 345, 440
Robertson, P., Roy, A., & Mahadevan, S. 2015, ApJL, 805, L22
Soto, M. G., & Jenkins, J. S. 2018, A&A, 615, A76
Standish, E. M., Jr. 1990, A&A, 233, 252
Stassun, K. G., & Torres, G. 2021, ApJL, 907, L33
Stromberg, G. 1939, ApJ, 89, 10
Subasavage, J. P., Bailyn, C. D., Smith, R. C., et al. 2010, Proc. SPIE, 7737, 77371C
Szebehely, V., & Zare, K. 1977, A&A, 58, 145
Timpe, M., Barnes, R., Kopparapu, R., et al. 2013, AJ, 146, 63
Tinney, C. G., Butler, R. P., Marcy, G. W., et al. 2001, ApJ, 551, 507
Trifonov, T., Tal-Or, L., Zechmeister, M., et al. 2020, A&A, 636, A74
Wittenmyer, R. A., Horner, J., Mengel, M. W., et al. 2017, AJ, 153, 167
Wittenmyer, R. A., Horner, J., Tinney, C. G., et al. 2014, ApJ, 783, 103
Wright, J. T., Upadhyay, S., Marcy, G. W., et al. 2009, ApJ, 693, 1084
Yong, D., & Lambert, D. L. 2003, PASP, 115, 796
Zechmeister, M., & Kürster, M. 2009, A&A, 496, 577